



Bifurcations in Morris–Lecar neuron model

Kunichika Tsumoto^{a,c,*}, Hiroyuki Kitajima^b,
Tetsuya Yoshinaga^c, Kazuyuki Aihara^{d,e}, Hiroshi Kawakami^f

^a*Department of Telecommunications, Takuma National College of Technology, 551 Koda,
Takuma, Kagawa 769-1192, Japan*

^b*Department of Reliability-based Information Systems Engineering, Faculty of Engineering,
Kagawa University, 2217-20, Hayashi-cho, Takamatsu 761-0396, Japan*

^c*Department of Radiologic Science and Engineering, School of Health Sciences, The University of
Tokushima, Tokushima, 3-18-15 Kuramoto, Tokushima 770-8509, Japan*

^d*Institute of Industrial Science, The University of Tokyo, 4-6-1 Komaba Meguro-ku,
Tokyo 153-8505, Japan*

^e*Aihara Complexity Modelling Project, ERATO, Japan Science and Technology Agency (JST),
3-23-5 August House 2F Uehara, Shibuya-ku, Tokyo, 151-0064, Japan*

^f*The University of Tokushima, 2-24, Shinkura, Tokushima 770-8501, Japan*

Received 22 December 2003; received in revised form 27 February 2005; accepted 2 March 2005

Available online 12 July 2005

Communicated by A. Borst

Abstract

The Morris–Lecar (M–L) equations are an important neuron model that exhibits classes I and II excitabilities when system parameters are set appropriately. Although many papers have clarified characteristic behaviors of the model, the detailed transition between two classes is unclear from the viewpoint of bifurcation analyses. In this paper, we investigate bifurcations of invariant sets in a five-dimensional parameter space, and identify an essential parameter of the half-activated potential of the potassium activation curve that contributes to the

*Corresponding author. Present address: Aihara Complexity Modelling Project, ERATO, Japan Science and Technology Agency (JST), 3-23-5 August House 2F Uehara, Shibuya-ku, Tokyo, 151-0064, Japan. Tel.: +81 3 5452 0371; fax: +81 3 5452 0377.

E-mail address: tsumoto@aihara.jst.go.jp (K. Tsumoto).

alternation of the membrane properties of the M–L neuron. We also show that the membrane property can be controlled by varying the value of the single parameter.

© 2005 Elsevier B.V. All rights reserved.

Keywords: Morris–Lecar model; Classes I and II neuron; Saddle-node bifurcation; Homoclinic bifurcation

1. Introduction

Various types of biophysical models have been proposed [1,28,33,41] for studying dynamical properties of biological membranes. Most of them are based on the Hodgkin–Huxley (H–H) type of equations that originally described the electrically excitable characteristics of the squid giant axons [16]. Generally, the neuron models are classified into two types, classes I and II, according to the difference of the onsets of repetitive firing [11,15,17,22,32]. Neurons with the class I excitability begin repetitive firing with an almost zero frequency. In contrast, class II neurons begin repetitive firing with a finite frequency. This difference can be explained by the bifurcation theory. The generation of the repetitive firing in the class I neuron results from a saddle-node bifurcation on an invariant circle. For example, the Morris–Lecar (M–L) model [26], the Hindmarsh–Rose model [14], and the Connor model [7] generate repetitive firing by a saddle-node bifurcation. While, subcritical Hopf bifurcations underlie the class II excitability. The original H–H [16] and the FitzHugh–Nagumo [9,27,31] models are the typical class II neurons.

Related to repetitive firing, physiological experiments [10,35,40] have reported different phenomena with synchronous firing observed in the real brain. To understand possible information processing, synchronization in coupled H–H models has been investigated [20,21,24,39,43]. However, many cortical neurons in mammals, such as pyramidal cells, are thought to possess the class I excitability. Hence, it is important to investigate synchronized responses in systems of coupled class I neurons.

When neural networks composed of a large number of coupled neurons are considered, a simple neuron model with less state variables like the M–L neuron model with two variables can have an advantage. Moreover, detailed knowledge of the dynamics of the single neuron model with class I excitability is desirable for studying synchronization phenomena observed in coupled neural systems.

For example, Rinzel and Ermentrout [32] studied mechanisms of bifurcations in the M–L neuron model by changing the externally applied DC current and found that the bifurcation in the generation of the repetitive firing changes from the saddle-node bifurcation to the subcritical Hopf bifurcation due to the variation of the system parameters. Namely, the M–L model can exhibit properties of classes I and II excitabilities [11,22]. Although, it is shown that the properties of the M–L model changes when the values of four parameters are simultaneously changed [11,32], it is not very clear which parameter change is dominantly related to the changes of properties in the M–L model.

Accordingly, in this paper, we analyze a global view of the bifurcation structure of the M–L neuron in the multiple-parameter space and clarify the essential parameter that contributes to the change of the membrane property of the model. We change various parameters of the M–L model over wide ranges, including previously studied parameters [11,32]. Paying much attention to the change in bifurcation structures between classes I and II, we analyze the bifurcation sets numerically and investigate two-parameter bifurcation diagrams with the applied DC current as the abscissa and the other parameter as the ordinate. Using bifurcation diagrams obtained from the analysis, we can identify parameter regions in which the M–L model behaves as the class I neuron. We also show that the membrane property of the M–L neuron can be controlled by changing the value of only one parameter.

This paper is organized as follows. The M–L neuron model is described in Section 2. In Section 3, bifurcation types considered in this paper and numerical methods are summarized. The results are shown in Section 4. Finally, the discussion and the conclusion are given in Section 5.

2. Model

2.1. Morris–Lecar neuron

The M–L neuron model [26], proposed as a model for describing a variety of oscillatory voltage patterns of Barnacle muscle fibers, is described by

$$\begin{aligned} C_M \frac{dV}{dt} &= -\bar{g}_L(V - V_L) - \bar{g}_{Ca}M_\infty(V - V_{Ca}) - \bar{g}_K N(V - V_K) + I_{\text{ext}}, \\ \frac{dN}{dt} &= \frac{N_\infty - N}{\tau_N}, \end{aligned} \quad (1)$$

where V is the membrane potential, $N \in [0, 1]$ is the activation variable for K^+ , I_{ext} is the externally applied DC current that is assumed to be temporally constant as a parameter and t denotes the time measured in milliseconds. The system parameters V_{Ca} , V_K , and V_L represent equilibrium potentials of Ca^{2+} , K^+ , and leak currents, respectively, and \bar{g}_{Ca} , \bar{g}_K , and \bar{g}_L denote the maximum conductances of corresponding ionic currents.

Because the Ca^{2+} current changes much faster than the K^+ current, we assume that the Ca^{2+} current is always in equilibrium with its activation curve, which is given by

$$M_\infty = 0.5[1 + \tanh\{(V - V_1)/V_2\}], \quad (2)$$

where V_1 is the midpoint potential at which the calcium current is half-activated, i.e., $M_\infty = 0.5$. Moreover we assume V_2 is a constant, corresponding to the steepness of the activation voltage dependence.

Table 1
Fixed parameters for the M–L neuron [11]

$C_M = 20$ ($\mu\text{F}/\text{cm}^2$)
$g_K = 8$ (mS/cm^2)
$g_L = 2$ (mS/cm^2)
$V_{\text{Ca}} = 120$ (mV)
$V_K = -80$ (mV)
$V_L = -60$ (mV)
$V_1 = -1.2$ (mV)
$V_2 = 18$ (mV)

The steady-state potassium activation N_∞ is also a voltage-dependent function defined as follows:

$$N_\infty = 0.5[1 + \tanh\{(V - V_3)/V_4\}], \quad (3)$$

where V_3 is the activation midpoint potential at which the potassium current is half-activated and V_4 denotes the slope factor of the potassium activation. In Eq. (1), we assume that the time constant τ_N with respect to the potassium activation is described by

$$\tau_N = 1/[\phi \cosh\{(V - V_3)/2V_4\}]. \quad (4)$$

In this paper, we treat I_{ext} as a main control parameter, and analyze two-parameter bifurcations in the parameter plane of I_{ext} and one of the parameters \bar{g}_{Ca} , ϕ , V_3 , and V_4 . The parameter values in Eqs. (1)–(4), except for I_{ext} , \bar{g}_{Ca} , ϕ , V_3 , and V_4 , are listed in Table 1 [11].

2.2. Nullclines

In order to understand how the system evolves with time, let us define two isoclines, each of which is a curve in the (V, N) plane, along which one of the derivatives is constant. In particular, the null isocline, or the nullcline, is the curve along which either dV/dt or dN/dt is zero. The V -nullcline associated with the fast variable V , defined by the set satisfying $dV/dt = 0$, is described by the following function:

$$N = \frac{I_{\text{ext}} - \bar{g}_L(V - V_L) - \bar{g}_{\text{Ca}}M_\infty(V - V_{\text{Ca}})}{\bar{g}_K(V - V_K)}. \quad (5)$$

The N -nullcline associated with the variable N , defined by the set satisfying $dN/dt = 0$, is a monotonically increasing function of V as follows:

$$N = 0.5[1 + \tanh\{(V - V_3)/V_4\}](\equiv N_\infty). \quad (6)$$

3. Analysis methods

In this section, we summarize methods for calculating various types of bifurcations in the M–L system.

Let us represent the two-dimensional autonomous differential equations composed of Eqs. (1)–(4) as follows:

$$\frac{dx}{dt} = f(x), \quad (7)$$

where $t \in R$ and $x \in R^2$ denote the time and the state vector, respectively.

3.1. Bifurcation of equilibrium point

In Eq. (7), a point x^* satisfying $f(x^*) = 0$ is an equilibrium point. The stability of the equilibrium point can be evaluated by linearizing the system around the equilibrium point and by computing eigenvalues of the Jacobian matrix. When we write the Jacobian matrix on the equilibrium point x^* as

$$Df(x^*) = \frac{\partial f(x^*)}{\partial x}, \quad (8)$$

the characteristic equation is given by

$$\det(\lambda_i I_2 - Df(x^*)) = \lambda_i^2 + a_1 \lambda_i + a_2 = 0, \quad (9)$$

where I_2 is the 2×2 identity matrix, λ_i 's with $i = 1, 2$ denote eigenvalues of the Jacobian matrix $Df(x^*)$. We call x^* a hyperbolic equilibrium point, if real parts of all eigenvalues are non-zero. A bifurcation of an equilibrium point occurs when the hyperbolicity of the equilibrium point is lost by the variation of a system parameter. Possible bifurcations of the equilibrium point appearing in the M–L neuron are as follows:

- (1) *The Hopf bifurcation:* Two eigenvalues in Eq. (9) are purely imaginary numbers. By changing the value of a parameter, an oscillatory solution appears.
- (2) *The saddle-node bifurcation:* One of the eigenvalues is zero. By changing the parameter value, a pair of equilibrium points appear.

The condition of each bifurcation can be described by a function of the coefficients in Eq. (9). The Hopf bifurcation curve is calculated from the condition $a_1 = 0$ and $a_2 > 0$. A parameter set satisfying $a_2 = 0$ becomes a curve of saddle-node bifurcations of equilibrium points.

3.2. Poincaré map and bifurcation of limit cycles

We consider a method for analyzing qualitative properties of limit cycles observed in Eq. (7). For this purpose, a geometric approach plays an effective role. Namely,

the qualitative analysis of Eq. (7) can be reduced to the study of a diffeomorphism, which we call the Poincaré map.

We assume that there exists a limit cycle solution in Eq. (7) with an initial condition $x = x_0$ at $t = t_0$, denoted by $x(t) = \varphi(t, x_0)$, for all t . We take a local section Σ which the solution crosses transversely as follows:

$$\Sigma = \{x \in R^2 \mid g(x) = 0\}, \quad (10)$$

where $g(x)$ is a scalar valued function of x in R^2 . In this paper, we define the cross-section

$$\Sigma = \{(V, N) \in R^2 \mid g(x) = V - V^* = 0, N < N^*\}, \quad (11)$$

where V^* and N^* denote the coordinate values of an equilibrium point x^* of the M–L system.

Let us define h as a local coordinate of Σ

$$h : \Sigma \rightarrow \Pi \subset R; x \mapsto \xi = h(x) \quad (12)$$

and its inverse h^{-1} as an embedding map

$$h^{-1} : \Pi \rightarrow \Sigma; \xi \mapsto x = h^{-1}(\xi), \quad (13)$$

where x satisfies $g(x) = 0$. Pick a point $x \in \Sigma$ and let $\Pi \subset \Sigma$ be some neighborhood of $\xi = h(x)$. Then the Poincaré map T is defined by the following composite map for a point $\xi \in \Pi$:

$$T : \Pi \rightarrow \Pi; \xi \mapsto h(\varphi(\tau(h^{-1}(\xi)), h^{-1}(\xi))), \quad (14)$$

where τ denotes the time in which the trajectory emanating from a point $x \in \Sigma$ will hit the local cross-section Σ again. The time τ is called a return time.

The fixed point of the Poincaré map T is given by

$$\xi - T(\xi) = 0. \quad (15)$$

We can obtain a one-to-one correspondence between the limit cycle of Eq. (7) and the fixed point of the Poincaré map T . Hence, the analysis of the limit cycle can be reduced to an analysis of the fixed point of the Poincaré map T .

Now, let $\xi^* \in \Sigma$ be a fixed point of T . Then the characteristic multiplier $\mu \in R$ is obtained by

$$\mu = \left. \frac{dT(\xi)}{d\xi} \right|_{\xi=\xi^*}. \quad (16)$$

Note that, by using Liouville's formula, the value of μ must be positive [30]. We call ξ^* a hyperbolic fixed point, if $\mu \neq 1$. The topological type of the hyperbolic fixed point can be classified by the distribution of the characteristic multiplier [18]. We have two topologically different types of hyperbolic fixed points, that is, ${}_0D$ and ${}_1D$ such that $0 < \mu < 1$ and $\mu > 1$, respectively.

Local and global bifurcations appearing in this paper are as follows:

- (1) *The tangent bifurcation:* This type of local bifurcation occurs when the condition with $\mu = 1$ is satisfied. By changing a parameter, a pair of fixed points appears.

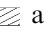

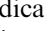
- (2) *The homoclinic bifurcation:* This global bifurcation is caused by the connection of stable and unstable manifolds of an equilibrium point. A closed orbit emerges with the variation of a system parameter.

The bifurcation sets in this paper were calculated by the fourth-order Runge–Kutta method with the double precision numbers. The numerical determination of the local bifurcation was accomplished using the method proposed by Kawakami [18]. On the other hand, for the calculation of the homoclinic bifurcation, we used the method in Refs. [19,42].

Before showing the results, we summarize notations about equilibrium points, limit cycles, and their bifurcations. For representing types of equilibrium points, we use the notation ${}_kO_s$ with $k = 0, 1, 2$, where the subscript integer k indicates the unstable dimension of the equilibrium point and s is used to distinguish multiple equilibrium points, if they coexist. On the other hand, the symbol ${}_kD$ with $k = 0, 1$, denotes a fixed point of the Poincaré map, where k denotes the unstable dimension of the fixed point. In bifurcation diagrams, we use the following notations: g_ℓ and h_ℓ for the saddle-node and the Hopf bifurcations of an equilibrium point, respectively, where ℓ indicates the number to distinguish the several same bifurcation sets if they exist; G_ℓ and H_ℓ for the tangent and the homoclinic bifurcations, respectively, where ℓ indicates the number to distinguish the same bifurcation sets as well.

4. Results

In this section, we show numerical results obtained by the bifurcation analysis of the M–L neuron with the fixed system parameter values denoted in Table 1.

Bifurcation diagrams in (I_{ext}, V_3) , $(I_{\text{ext}}, \bar{g}_{\text{Ca}})$, (I_{ext}, ϕ) , and (I_{ext}, V_4) -planes are shown in Figs. 1(a)–(d), respectively. In each diagram, the parameters, except for a couple of parameters of the coordinate system, are fixed as values for a class I neuron model as shown in Table 2. In the bifurcation diagrams, the regions  and  denote the parameter regions in which a stable limit cycle and three equilibrium points exist, respectively, and the shading pattern  in Fig. 1(c) and (d) indicates the regions of tristability, meaning coexistence of two stable equilibrium points and a stable limit cycle. In the following, we consider bifurcation phenomena observed in each parameter plane.

4.1. Bifurcations in the (I_{ext}, V_3) -plane

We consider typical bifurcations related to a generation of a limit cycle, which corresponds to emergence of repetitive firing. First, we account for each bifurcation mechanism along lines ℓ_1 and ℓ_2 in Fig. 1(a).

Fig. 2(a) shows a one-parameter bifurcation diagram along the line ℓ_1 in Fig. 1(a). When the externally applied DC current I_{ext} is increased, the stable and the saddle equilibrium points denoted by symbols ${}_0O_L$ and ${}_1O_M$ in Fig. 2(a), respectively, get closer to each other. At the saddle-node bifurcation g_1 , two equilibrium points

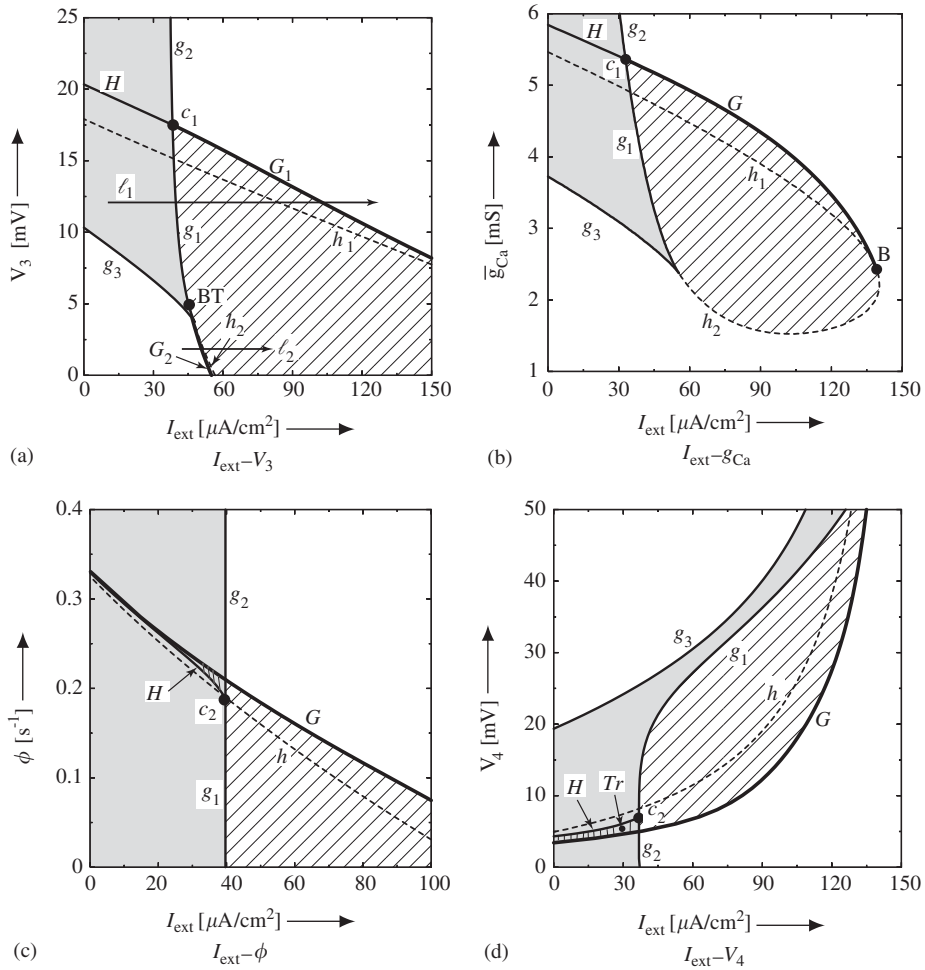


Fig. 1. Bifurcation diagrams for equilibrium points and a limit cycle. Parameters except for the coordinate system are fixed to values for a class I neuron model as shown in Table 2. Region hatched indicates parameters at which a stable limit cycle exists. In parameter region shaded , three equilibrium points coexist.

Table 2
System parameters for classes I and II models [11,32]

Parameter	Class I	Class II
g_{Ca} (mS/cm ²)	4.0	4.4
ϕ (s ⁻¹)	$\frac{1}{15}$	$\frac{1}{25}$
V_3 (mV)	12	2
V_4 (mV)	17.4	30

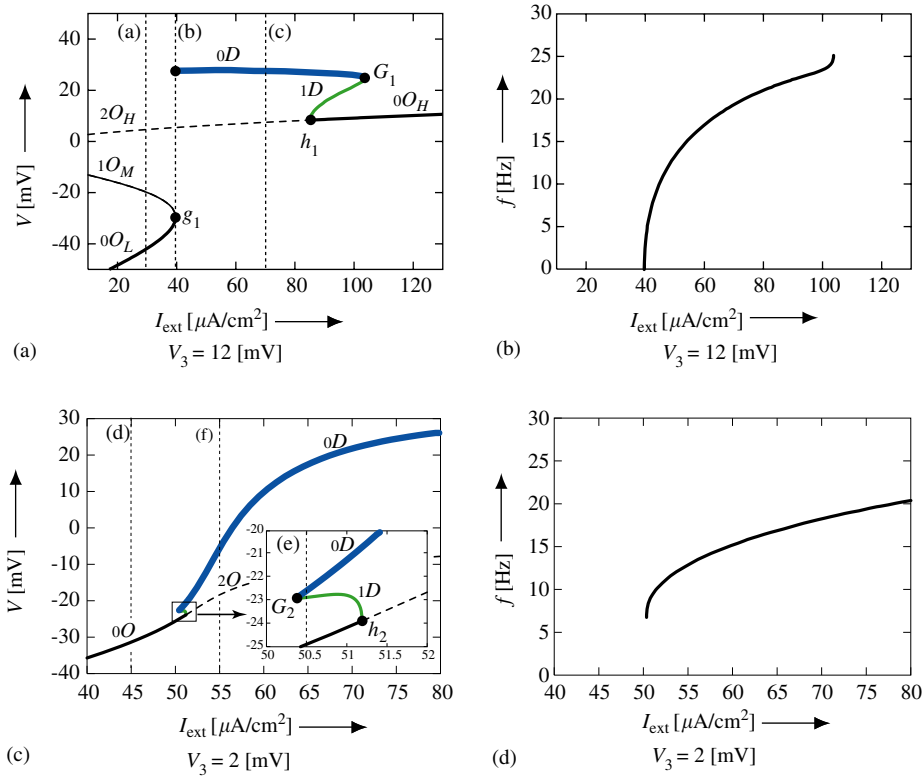


Fig. 2. (a), (c) One-parameter bifurcation diagrams and (b), (d) graphs of frequency f as a function of I_{ext} , where $V_3 = 12$ mV in (a) and (b), and $V_3 = 2$ mV in (c) and (d). In each one-parameter bifurcation diagram, symbols ${}_k O_s$, with $k = 0, 1, 2$, $s = L, M, H$, and ${}_k D$, with $k = 0, 1$, indicate equilibrium points and limit cycles.

coalesce and disappear. After the saddle-node bifurcation g_1 , we can see a generation of a limit cycle with type ${}_0 D$. Phase portraits and waveforms before and after the saddle-node bifurcation g_1 are illustrated in Figs. 3(a)–(c). Note that the values of I_{ext} labeled by (a)–(c) in Fig. 2(a) correspond to the phase portraits shown in Figs. 3(a)–(c), respectively. On the other hand, a one-parameter bifurcation diagram along the line ℓ_2 in Fig. 1(a) is shown in Fig. 2(c). If I_{ext} is relatively small, then the M–L neuron has a stable equilibrium point with type ${}_0 O$, an example of which is shown in Fig. 3(d). By increasing I_{ext} , a pair of limit cycles is generated by the tangent bifurcation G_2 as shown in Fig. 2(c). The generated limit cycle with type ${}_0 D$ corresponds to repetitive firing in the M–L neuron. Consequently, the stable limit cycle ${}_0 D$ coexists with the stable equilibrium point with type ${}_0 O$. Namely, there is bistability in the narrow range between the tangent bifurcation G_2 and the Hopf bifurcation h_2 in Fig. 2(c). An example of bistability observed at the point labeled by

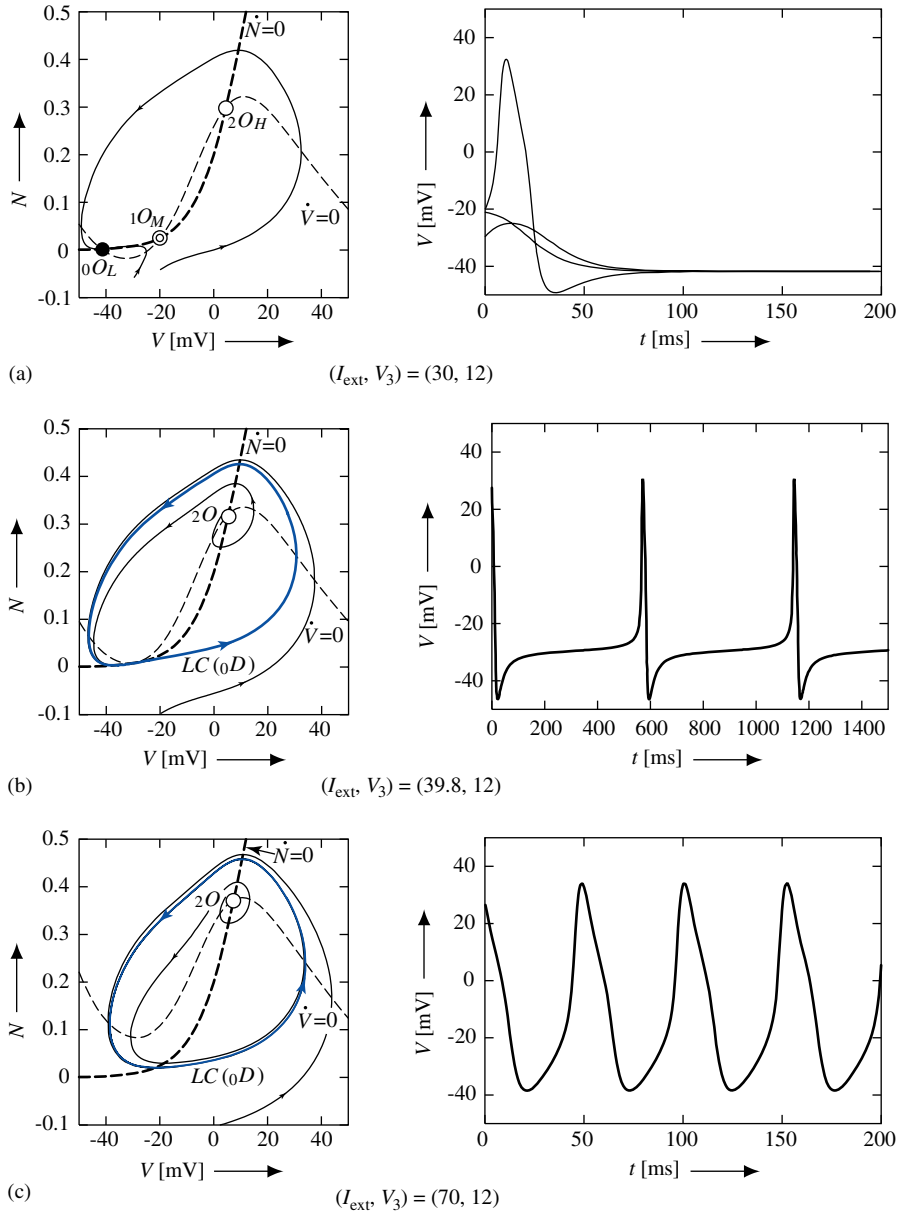


Fig. 3. Examples of attractors observed in Eq. (1). (Left) Phase portraits. (Right) Waveforms. In phase portraits, black, white, and double circles denote stable, spiral source, and saddle equilibrium points. Arrows indicate directions of trajectories. Blue and green closed curves denote stable and unstable limit cycles. Light and heavy dashed curves indicate V - and N -nullclines of Eqs. (5) and (6).

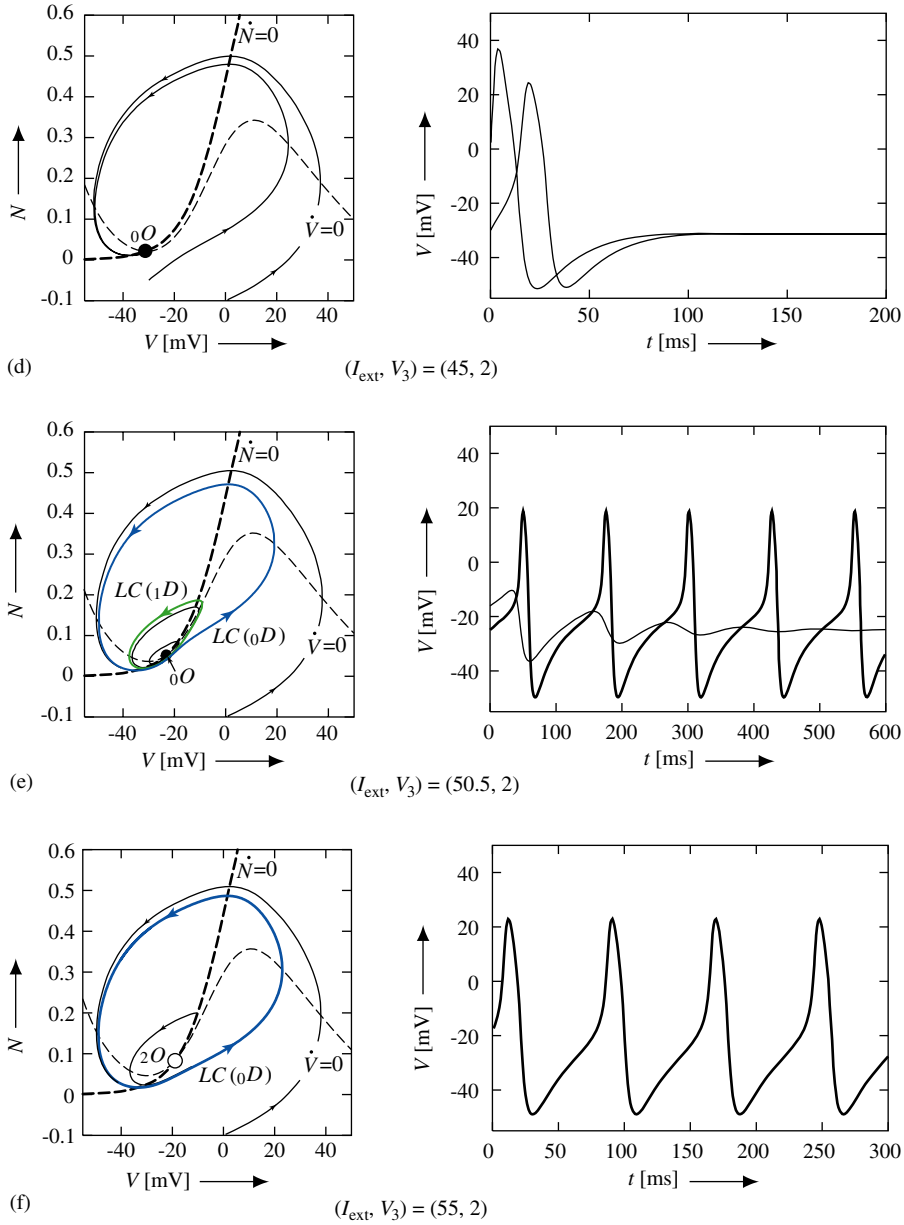


Fig. 3. (Continued)

(e) in Fig. 2(c) is shown in Fig. 3(e). By further increasing I_{ext} , we observe a subcritical Hopf bifurcation h_2 with the following formula:

$${}_0O + {}_1D \rightarrow {}_2O, \quad (17)$$

where the left- and right-hand sides of the arrow show equilibrium points and a limit cycle before and after the bifurcation, respectively. After the Hopf bifurcation h_2 , the stable limit cycle with type ${}_0D$ remains a unique attractor (see Fig. 3(f)).

Next, let us consider bifurcation phenomena around the point labeled c_1 in Fig. 1(a). Fig. 4 shows an enlarged bifurcation diagram near the point c_1 in Fig. 1(a), while relevant phase portraits are presented in Fig. 5. We can explain various transitions between an equilibrium state and a periodic firing state emerging by passing through each bifurcation curve in Fig. 4. We suppose that the values of parameters I_{ext} and V_3 vary across bifurcation sets as in the following cases:

Case 1: ① \rightarrow ② $\rightarrow H \rightarrow$ ③

As the first bifurcation, we observe a subcritical Hopf bifurcation h_1 related to a spiral source of an equilibrium point ${}_2O_H$. The bifurcation formula is given by

$${}_2O_H \rightarrow {}_0O_H + {}_1D. \quad (18)$$

The unstable limit cycle with type ${}_1D$, which is generated by the Hopf bifurcation h_1 , approaches the saddle equilibrium point ${}_1O_M$ by further increasing V_3 , and then a homoclinic orbit is generated at the bifurcation point H (see the panel H in Fig. 5). After the homoclinic bifurcation H , the unstable limit cycle disappears as shown in panel ③ in Fig. 5.

Case 2: ④ \rightarrow ⑤ \rightarrow ⑥

At the parameter value labeled by ④ in Fig. 4, there is a stable limit cycle with type ${}_0D$ and a spiral source of an equilibrium point ${}_2O_H$. By increasing V_3 from ④ to ⑤, we observe the Hopf bifurcation h_1 . At Hopf bifurcation h_1 , the stability of the equilibrium point ${}_2O_H$ changes, and then an unstable limit cycle with type ${}_1D$ appears, as shown in panel ⑤ in Fig. 5. A tangent bifurcation of limit cycles occurs when the value of V_3 crosses the bifurcation set G_1 by further increasing V_3 . The

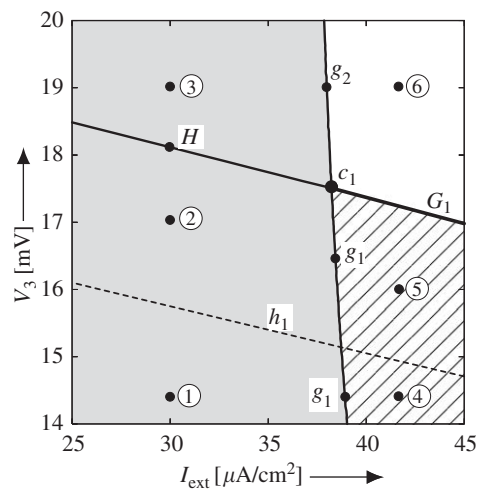


Fig. 4. An enlarged bifurcation diagram around the parameter point labeled by c_1 in Fig. 1(a).

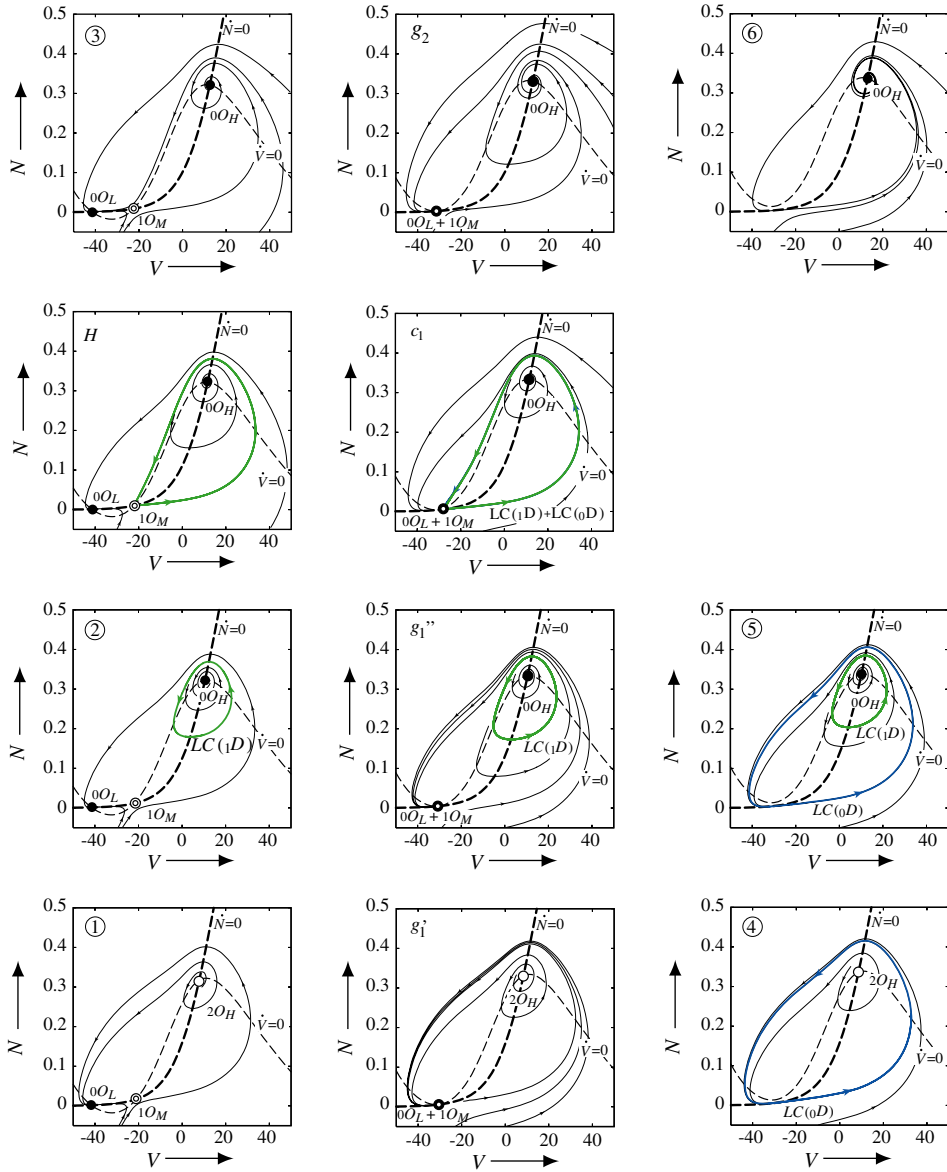


Fig. 5. Examples of various phase portraits observed at points labeled by numbers with circle and bifurcation symbols in Fig. 4. The number with circle or the bifurcation symbols in each phase portrait correspond to those in Fig. 4.

bifurcation formula is given by

$${}_0D + {}_1D \rightarrow \Phi, \quad (19)$$

where the symbol Φ denotes the disappearance of a pair of the stable and the unstable limit cycles. Panel ⑥ in Fig. 5 shows an example of a phase portrait after the tangent bifurcation G_1 .

Case 3: ① $\rightarrow g'_1 \rightarrow$ ④

By increasing I_{ext} , the stable and the saddle equilibrium points get closer to each other. At the saddle-node bifurcation g'_1 , two equilibrium points coalesce and disappear. After the saddle-node bifurcation g'_1 , the stable limit cycle with type ${}_0D$ exists. Note that the mechanism of the genesis of the limit cycle is the same as that of the bifurcation mechanism along the line ℓ_1 in Fig. 1(a).

Case 4: ② $\rightarrow g''_1 \rightarrow$ ⑤

In the point labeled by ② in Fig. 4, two stable equilibrium points ${}_0O_L$ and ${}_0O_H$ coexist as attractors. Moreover, an unstable limit cycle exists since the value of V_3 is larger than that of the Hopf bifurcation h_1 . By increasing I_{ext} , we observe the saddle-node bifurcation g''_1 . Due to this saddle-node bifurcation g''_1 , the stable and the saddle equilibrium points ${}_0O_L$ and ${}_1O_M$ coalesce and disappear, and a stable limit cycle with type ${}_0D$ appears according to the same mechanism of case 3. After the saddle-node bifurcation g''_1 , we can see a typical phenomenon of bistability of the stable equilibrium point ${}_0O_H$ and the stable limit cycle ${}_0D$.

Case 5: ③ $\rightarrow g_2 \rightarrow$ ⑥

When the value of I_{ext} varies across the bifurcation set g_2 in the direction from ③ to ⑥, we observe the following bifurcations:

$${}_0O_L + {}_1O_M \rightarrow \Phi \quad (20)$$

Note that a generation of a limit cycle is not observed after the saddle-node bifurcation g_2 .

It should be noted that a degenerated bifurcation occurs at the point labeled by c_1 in Fig. 4. At point c_1 , the saddle-node bifurcation of equilibrium points, the homoclinic bifurcation, and the tangent bifurcation of limit cycles occur simultaneously (see the panel c_1 in Fig. 5).

Finally, we consider bifurcation phenomena observed around the point labeled by BT in Fig. 1(a). Fig. 6 shows enlarged and detailed bifurcation diagrams near the bifurcation point BT in Fig. 1(a). At the saddle-node bifurcation g_3 , a saddle and a nodal source of equilibrium points coalesce and disappear. When the values of I_{ext} and V_3 across the saddle-node bifurcation set g_3 in the direction from inside to outside the region \square , the number of equilibrium points changes from three to one. Unlike the saddle-node bifurcation g_1 , a limit cycle does not emerge with the bifurcation g_3 . After the saddle-node bifurcation g_3 , a stable equilibrium point remains as a unique attractor. On the other hand, the bifurcation set g_6 forms a cusp point, which is labeled by CP in Fig. 6(a), together with the saddle-node bifurcation set g_4 of equilibrium points. At the cusp point CP , nodal source of two equilibrium points and a saddle coalesce into one nodal point. The Hopf bifurcation set h_2 is terminated on the saddle-node bifurcation sets composed of g_1 and g_4 . At this value of the termination, there is an equilibrium point with double zero eigenvalues. Moreover, the homoclinic bifurcation curve H_3 originates from the terminated point

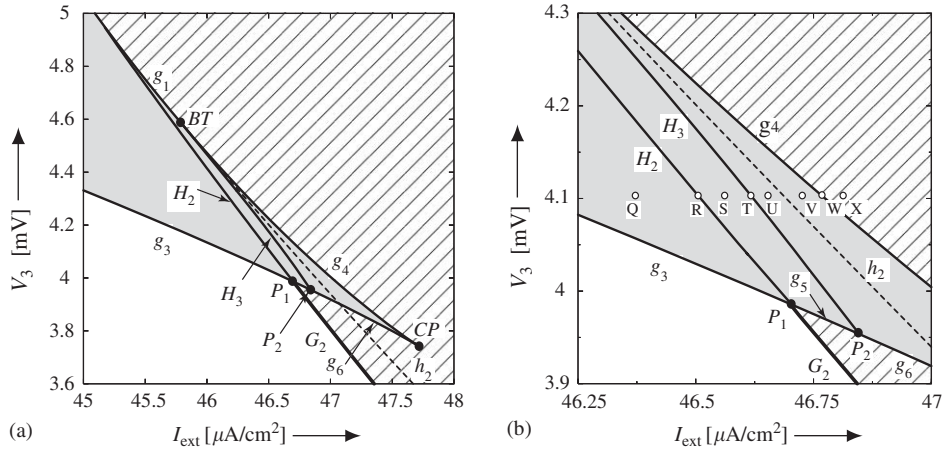


Fig. 6. Enlarged bifurcation diagrams. Panel (a) is an enlarged diagram around the Bogdanov–Takens bifurcation point [2,23,37] labeled by *BT* in Fig. 1(a). Panel (b) denotes an enlarged diagram around point P_1 in panel (a).

of the Hopf bifurcation set h_2 . Thus, the system exhibits the generic Bogdanov–Takens (BT) bifurcation [2,23,37] at this point.

In the following, we summarize bifurcation mechanisms related to geneses of limit cycles. Fig. 6(b) shows an enlarged bifurcation diagram around the homoclinic bifurcation set H_3 in Fig. 6(a). The points labeled by Q – X show parameter values at which the attractors shown in Figs. 7(a)–(h) are observed, respectively. When the value of I_{ext} increases between the points Q and S , for the fixed value of V_3 equal to 4.1 mV, a homoclinic orbit emerges at point R . The orbit along one of the unstable manifolds of the saddle equilibrium point ${}_1O_M$ agrees with that along one of the stable manifolds, encircling equilibrium points ${}_2O_H$ and ${}_0O_L$ as shown in Fig. 7(b). The homoclinic orbit is destroyed by increasing I_{ext} , and a stable limit cycle appears as shown in Fig. 7(c). By further increasing I_{ext} , we observe another kind of homoclinic bifurcation H_3 at point T in Fig. 6(b). After the homoclinic bifurcation H_3 , the homoclinic orbit generates an unstable limit cycle. The unstable limit cycle with ${}_1D$, which emerges after the homoclinic bifurcation H_3 , disappears at the Hopf bifurcation h_2 . Before and after the Hopf bifurcation h_2 , we have the following bifurcation formula:

$${}_0O_L + {}_1D \rightarrow {}_2O_L. \quad (21)$$

The transition is illustrated in Figs. 7(e) and (f). A saddle-node bifurcation of equilibrium points is observed when I_{ext} crosses the bifurcation set g_4 with further increasing I_{ext} . Figs. 7(f)–(h) correspond to the phase portraits observed before and after the saddle-node bifurcation g_4 . On the other hand, it should be noted that degenerate bifurcations occur at points labeled by P_1 and P_2 in Fig. 6(a) and (b) such that each homoclinic bifurcation set is terminated on a saddle-node bifurcation set. Figs. 8(a) and (b) show schematic phase portraits at points P_1 and P_2 in Fig. 6(a) and

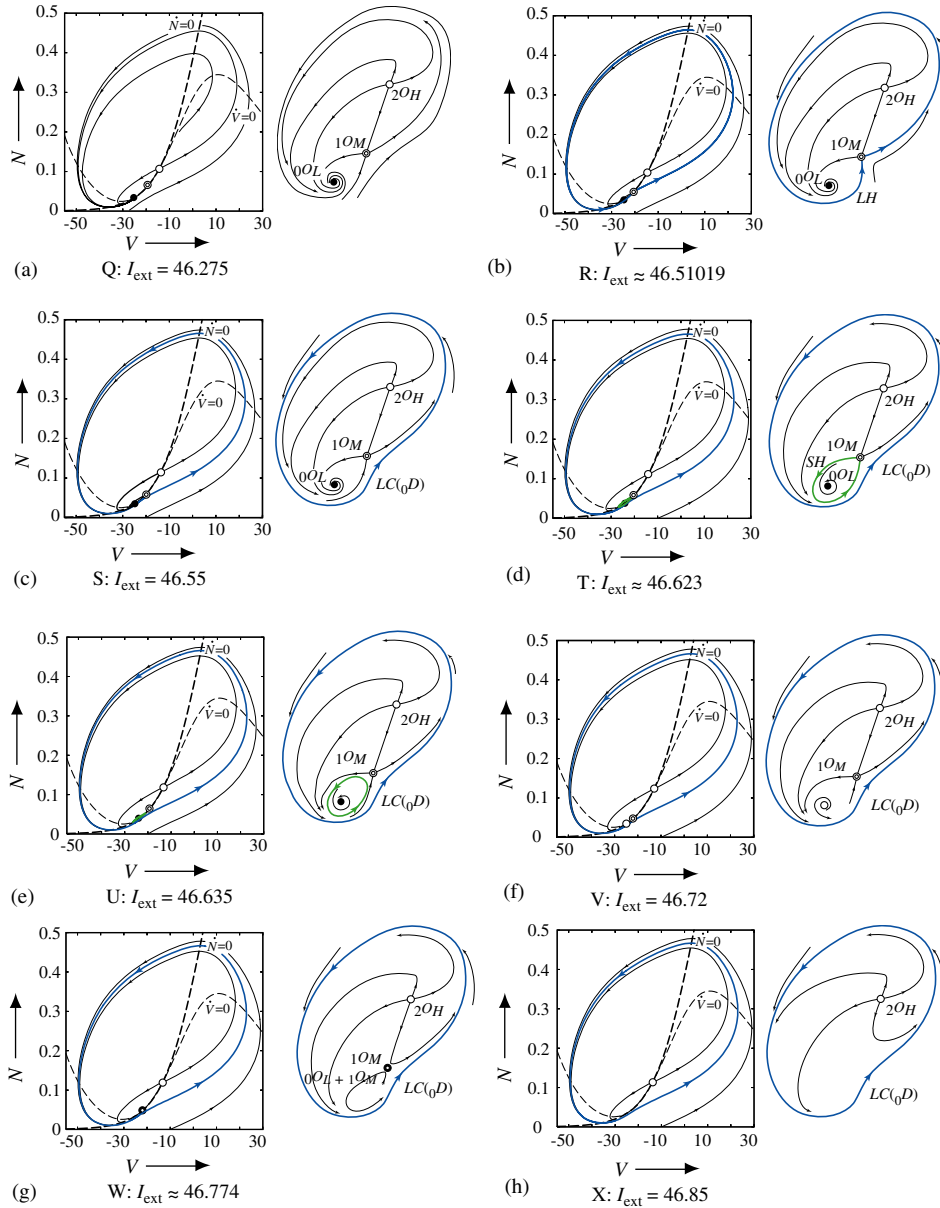


Fig. 7. Examples of phase portraits observed at points labeled by Q–X in Fig. 6(b). (Left) Phase portraits. (Right) Schematic diagrams of corresponding phase portraits. In each schematic diagram, symbols ${}_k O_\ell$, with $k = 0, 1, 2$, $\ell = L, M, H$, and $LC_k(D)$, with $k = 0, 1$, denote equilibrium points and limit cycles. Symbols SH and LH indicate small and large homoclinic orbits. $V_3 = 4.1$.

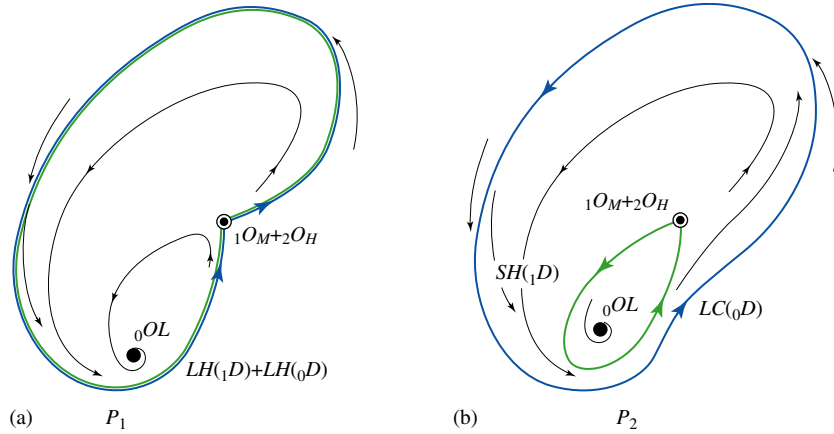


Fig. 8. Schematic diagrams of phase portraits observed at points P_1 and P_2 in Fig. 6. Symbols LH and SH indicate large and small homoclinic orbits.

(b), respectively. At each phase portrait, the saddle-node bifurcation with a saddle and a nodal source of equilibrium points and each type of homoclinic bifurcations occur simultaneously. Furthermore, at point P_1 , the homoclinic bifurcation related to an unstable limit cycle also occurs simultaneously. Note that the unstable limit cycle is generated by passing through the bifurcation set g_5 in the direction from inside to outside the region \square . The bifurcation mechanism of the genesis of the unstable limit cycle is the same as that in the case of the saddle-node bifurcation g_1 .

4.2. Bifurcations in the $(I_{\text{ext}}, \bar{g}_{\text{Ca}})$ -plane

Fig. 1(b) shows a bifurcation diagram of equilibrium points and limit cycles in the $(I_{\text{ext}}, \bar{g}_{\text{Ca}})$ -plane. Except for the Hopf bifurcation h_2 , each bifurcation labeled by the same symbol as in Fig. 1(a) has the qualitatively similar mechanism described in the previous subsection. Hence, we consider the bifurcations related to the Hopf bifurcation h_2 . The tangent bifurcation set G emanates from the c_1 point and terminates at another point of the parameter space with the Hopf bifurcation set. Namely, the terminated point labeled by B in Fig. 1(b) denotes the Bautin bifurcation point [23] at which the Hopf bifurcation of an equilibrium point and the tangent bifurcation G of limit cycles occur simultaneously. At bifurcation point B , the Hopf bifurcation curve is divided into two curves with different properties: curve h_1 with a subcritical Hopf bifurcation and curve h_2 with a supercritical Hopf bifurcation. When the value of I_{ext} and \bar{g}_{Ca} vary across the bifurcation set h_2 in the direction from outside to inside the region \square , we observe the supercritical Hopf bifurcation with the following formula:

$${}_0O \rightarrow {}_2O + {}_0D. \quad (22)$$

Note that the limit cycle generated by the supercritical Hopf bifurcation h_2 arises with an arbitrarily small amplitude.

4.3. Bifurcations in the (I_{ext}, ϕ) -plane

Let us consider bifurcations in the (I_{ext}, ϕ) -plane. In Fig. 1(c), it should be noted that the parameter region in which two stable equilibrium points and a stable limit cycle coexist, denoted by $\square\square\square$, appears due to the variation of ϕ . Namely, we can observe the phenomenon of tristability. In the following, we show a mechanism of the bifurcation process that enables the generation of the tristability. An enlarged bifurcation diagram near point c_2 in Fig. 1(c) is shown in Fig. 9. Figs. 10(a)–(d) show schematic one-parameter bifurcation diagrams along the lines ℓ_3^k , for $k = 1, 2, 3$, and 4, in Fig. 9. As shown in Fig. 10(a), the mechanism of the generation of the stable limit cycle when I_{ext} increases along the line ℓ_3^1 is the same as those in the (I_{ext}, V_3) —and the $(I_{\text{ext}}, \bar{V}_{\text{Ca}})$ —planes; an example of the one-parameter bifurcation diagram is shown in Fig. 2(a). When the parameter I_{ext} changes along line ℓ_3^2 in Fig. 9, a degenerated bifurcation at point c_2 is observable. At point c_2 , the saddle-node bifurcation of equilibrium points and the homoclinic bifurcation H occur simultaneously. By increasing the value of ϕ , the parameter value of the generation of the homoclinic bifurcation H is shifted in the direction of decreasing the value of I_{ext} . The point c_2 in Fig. 9 is the border of the parameter value of ϕ such that the bifurcation mechanism related to the generation of a stable limit cycle changes from the saddle-node bifurcation to the homoclinic one. Moreover, the bifurcation processes along lines ℓ_3^3 and ℓ_3^4 in Fig. 9 are explained as follows. When the value of I_{ext} passes through the Hopf bifurcation curve h , the stability of the spiral source ${}_2O_H$ changes. The bifurcation formula is given by

$${}_2O_H \rightarrow {}_0O_H + {}_1D \quad (23)$$

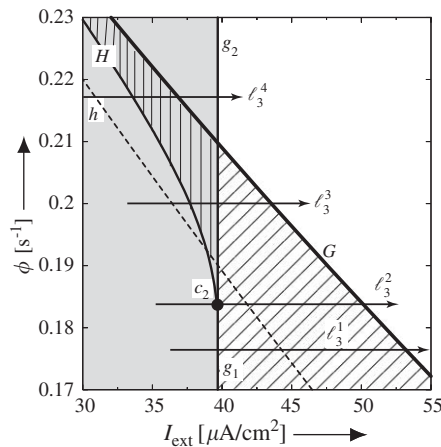


Fig. 9. Enlarged bifurcation diagram of Fig. 1(c).

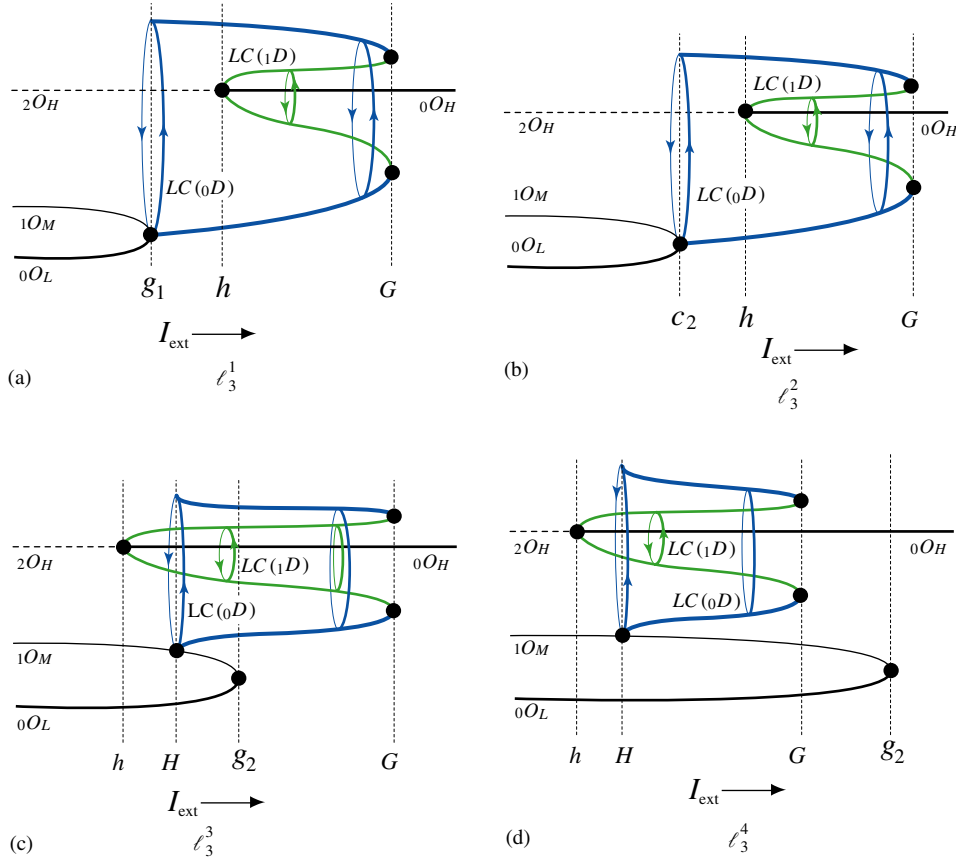


Fig. 10. Schematic one-parameter bifurcation diagrams along lines ℓ_3^k , for $k = 1, 2, 3$, and 4 , in Fig. 9(c). Heavy solid, light solid, and dashed curves indicate stable, saddle, and spiral source equilibrium points. Blue and green curves denote stable and unstable limit cycles. Symbols h, g_1, g_2, H , and G are identical to those in Fig. 9.

in the direction of increasing the value of I_{ext} . By further increasing I_{ext} , the saddle equilibrium point $1O_M$ is subjected to the homoclinic bifurcation H , and then a stable limit cycle appears. After the homoclinic bifurcation H , we can observe the tristability phenomenon such that two stable equilibrium points $0O_L$ and $0O_H$ and the stable limit cycle generated by the homoclinic bifurcation H coexist. The stable limit cycle disappears at the tangent bifurcation G , together with the unstable limit cycle, which is generated by the Hopf bifurcation of Eq. (23). Note that the phenomenon of the tristability can be observed in the range of parameters between the homoclinic bifurcation H and the saddle-node bifurcation g_2 (resp., tangent bifurcation point G) with the change along the line ℓ_3^3 (resp., ℓ_3^4). These parameter ranges correspond to the region $\square\square\square$ in Fig. 1(c) or Fig. 9.

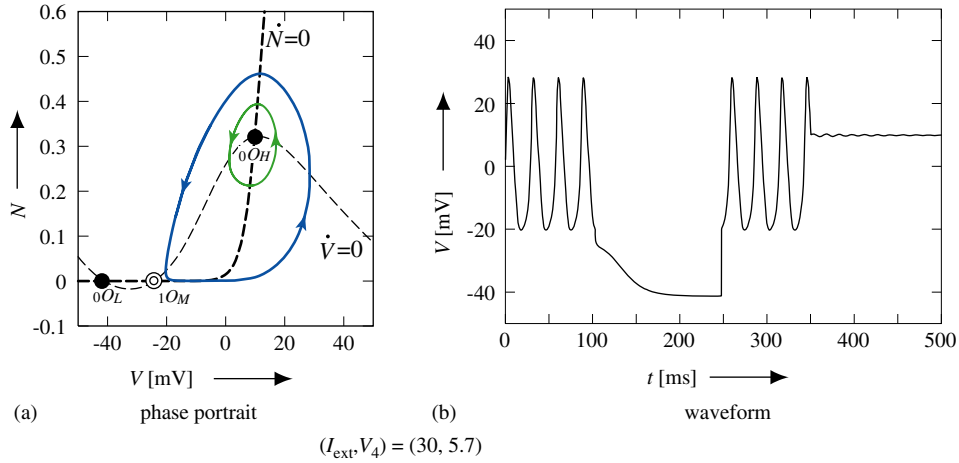


Fig. 11. Example of tristability observed at parameter point labeled by Tr in region $\square\square$ in Fig. 1(d). In the phase portrait (a), two nullclines intersect each other at three points representing steady states: a lower stable equilibrium point (${}_0O_L$), a saddle point (${}_1O_M$), and an upper stable equilibrium point (${}_0O_H$). Blue and green closed curves indicate stable and unstable limit cycles. The waveform (b) demonstrates transitions among three attractors.

4.4. Bifurcations in the (I_{ext}, V_4) -plane

Finally, we consider bifurcations in the (I_{ext}, V_4) -plane. According to the same mechanism described in the previous subsections, stable limit cycle is generated by varying the values of I_{ext} and V_4 through the bifurcation set g_1 in the direction from inside to outside the region \square in Fig. 1(d). On the other hand, it should be noted that a different type of a stable limit cycle generated via a homoclinic bifurcation can be observed in a certain parameter region. The homoclinic bifurcation is generated by decreasing the value of V_4 , passing through the curve H in Fig. 1(d). The bifurcation mechanisms observed at around the point labeled as c_2 in Fig. 1(c). In the region $\square\square$ in Fig. 1(d), we observe a phenomenon of the tristability, which may be meaningful as nerve dynamics. An example of the phase portrait and the waveform in a situation of the tristability is shown in Figs. 11(a) and (b), respectively. Fig. 11(b) shows transitions among three attractors caused by input perturbations to the variable V with appropriate timing.

5. Discussion

We have investigated bifurcations observed in the M–L neuron model. By analysing bifurcations by changing I_{ext} , \bar{g}_{Ca} , ϕ , V_3 , and V_4 , we have identified the parameter regions in which the M–L neuron exhibits properties of the class I

excitability, the bistability, and the tristability with the existence of two stable equilibrium points and one stable limit cycle.

In this section, we discuss the change in properties between classes I and II neurons. In particular, we focus on whether the membrane property can switch between two classes if a single parameter is changed. Rinzel and Ermentrout [32] studied stable solutions observed in the M–L model by changing the system parameters ϕ , \bar{g}_{Ca} , V_3 , and V_4 , and presented that the membrane properties of classes I and II correspond to repetitive firing oscillations generated by a saddle-node and a subcritical Hopf bifurcations of equilibrium points, respectively. However, the mechanism of the global transition between two classes is still unclear from the bifurcational point of view. Therefore we have investigated detailed bifurcations of invariant sets in the parameter space $(I_{ext}, \phi, \bar{g}_{Ca}, V_3, V_4)$. To identify the most important single parameter contributing to the membrane properties, we had the following strategy. First, we took the parameter values listed in Table 2, which are the same as considered in Ref. [11], namely we can observe that the neuron exhibits the class I excitability. Then, by using our method for bifurcation analysis, we calculated various kinds of planar bifurcation diagrams for the values of three parameters fixed above, and investigated a route to the class II excitability through bifurcation.

As shown in Figs. 1(a)–(d), repetitive firing is caused by the saddle-node bifurcation g_1 . This means the repetitive firing starts with the zero frequency. Indeed, from the graph of the frequency as a function of the parameter I_{ext} , shown in Fig. 2(b), the M–L neuron exhibits the property of the class I excitability. On the other hand, in the case of bifurcations observed in the (I_{ext}, V_3) -plane, when the value of I_{ext} is changed, e.g., along the line ℓ_2 in Fig. 1(a), the repetitive firing with a non-zero frequency appears via the subcritical Hopf bifurcation, see Figs. 2(c) and (d). This is the typical property of class II neurons. Among four bifurcation diagrams of Fig. 1, the only parameter plane including the route to class II excitability is (I_{ext}, V_3) . This result implies that the essential parameter determining the property of the membrane excitability of the M–L neuron is V_3 , which denotes the half-activated potential of the potassium activation curve.

Note that our investigation is based on the parameter setting by Rinzel and Ermentrout [32]. We can also observe different bifurcations by changing each bifurcation parameter over a wider range. For example, we observe a continuous transition from an equilibrium point to a limit cycle by the supercritical Hopf bifurcation h_2 in the (I_{ext}, \bar{g}_{Ca}) -plane when the value of \bar{g}_{Ca} is relatively small. Then, the limit cycle emerges with a non-zero frequency and a small amplitude, that is, the limit cycle corresponds to a non-firing subthreshold oscillation. By increasing the values of I_{ext} and \bar{g}_{Ca} , the oscillation of the limit cycle, which is generated by the Hopf bifurcation h_2 , continuously goes from non-firing to firing. In this case, the M–L model possess the property of the class II neuron in the sense that the firing oscillation starts with the non-zero frequency. While, the classification of repetitive firing based on the frequency as an oscillation termination has been proposed by Izhikevich [17]. Following Izhikevich's classification, the M–L neuron also has properties of the class II spiking.

It is thought that the presence of an A-current, which is known as a transient potassium current [6], plays a major role in the determination of the property of the nerve excitability. Therefore, it was widely believed that the original H–H model [16] does not exhibit the class I excitability unless the potassium A-current is added [6]. Rush and Rinzel [34] have shown, however, that an A-current is not necessary for the class I excitability if the sodium and potassium (in) activation curves in the H–H model are shifted appropriately. While, in the M–L model without the potassium A-current, the variation of the parameter V_3 corresponds to a shift on the potassium activation curve in the (V, N) plane. Therefore our result suggests that, in a general neuron model, the membrane property of classes I and II can be changed by shifting the potassium activation curve.

There are several studies related to analyses of coupled systems of class I neurons. Hansel et al. [12] reported that a synchronized repetitive firing does not appear and an anti-phase synchronization and cluster states can be observed in a class I neuron model coupled through the chemical synapse [8,12]. Nomura et al. [29] studied the effect of the synchronized firings on the variation of synapse conductances in coupled systems composed of a class I neuron with the chemical and the electrical synapses, and demonstrated that a synchronized repetitive firing and an anti-synchronized one coexist, depending on the initial condition. The result obtained in this paper will be useful in considering the difference of the spatio-temporal firing activities between two coupled systems consisting of the M–L neuron with distinct classes because the property of the membrane excitability can be controlled by only one-parameter variation of the half-activated potential of the potassium activation curve. From a physiological point of view, it might be difficult to directly test the change of properties of a nerve membrane by changing the activation curve of a potassium channel because the potassium activation is determined by the nature of the ion channel. However, advances in molecular biology, genetics, biochemistry, and physiology have been clarifying the structures of ion channels [4,36]; e.g., there are various kinds of potassium channels in nerve membranes [13]. In addition, it has recently been reported that the voltage dependence of the (in) activation of a certain potassium channel can be shifted by modulating a channel protein by a kinase, a phosphatase, etc. [3,5,25,38]. If the (in) activation curve of a potassium channel is appropriately shifted by modulating the channel protein, it may be possible to alter the property of the nerve membrane between classes I and II. Then, bifurcation analysis based on our numerical method will be feasible for investigating bifurcation structures related to the difference of neuron classes. Analysis of bifurcations in coupled systems of class I neurons with anatomically plausible connections is an important future problem.

Acknowledgements

The authors would like to thank Dr. S. Tsuji of the University of Tokushima, and Dr. K. Morita of the University of Tokyo for their insightful suggestions and fruitful discussions. This work was partially supported by the Grant-in-Aid for Young

Scientists (B) and the Grant-in-Aid on priority areas (C), Advanced Brain Science Project of the Ministry of Education, Science, Sports and Culture of Japan.

References

- [1] R.H. Adrian, W.K. Chandler, A.L. Hodgkin, Voltage clamp experiments in striated muscle fibers, *J. Physiol. (London)* 208 (1970) 607–644.
- [2] R.I. Bogdanov, Versal deformations of a singular point on the plane in the case of zero eigenvalues, *Funct. Anal. Appl.* 9 (1975) 144–145.
- [3] F.S. Cayabyab, F.W. Tsui, L.C. Schlichter, Modulation of the ERG K^+ current by the tyrosine phosphatase, SHP-1, *J. Biol. Chem.* 277 (50) (2002) 48130–48138.
- [4] S. Choe, Potassium channel structures, *Nat. Rev. Neurosci.* 3 (2002) 115–121.
- [5] I. Chung, L.C. Schlichter, Regulation of native Kv1.3 channels by cAMP-dependent protein phosphorylation, *Am. J. Physiol. Cell. Physiol.* 273 (1997) 622–633.
- [6] J.A. Connor, C.F. Stevens, Prediction of repetitive firing behavior from voltage-clamped data on an isolated neuron soma, *J. Physiol. (London)* 214 (1971) 31–53.
- [7] J.A. Connor, D. Walter, R. Mckown, Neural repetitive firing: modifications of the Hodgkin–Huxley axon suggested by experimental results from crustacean axons, *Biophys. J.* 18 (1977) 81–102.
- [8] B. Ermentrout, Type I membranes, Phase resetting curves, and synchrony, *Neural Comput.* 8 (1996) 979–1001.
- [9] R. FitzHugh, Impulses and physiological state in theoretical models of nerve membrane, *Biophys. J.* 1 (1961) 445–467.
- [10] C.M. Gray, P. Konig, A.K. Engel, W. Singer, Oscillatory responses in the cat visual cortex exhibit inter-columnar synchronization which reflects global stimulus properties, *Nature* 338 (23) (1989) 334–337.
- [11] B.S. Gutkin, G.B. Ermentrout, Dynamics of membrane excitability determine interspike interval variability: a link between spike generation mechanisms and cortical spike train statistics, *Neural Comput.* 10 (1998) 1047–1065.
- [12] D. Hansel, G. Mato, C. Meunier, Synchrony in excitatory neural networks, *Neural Comput.* 7 (1995) 307–335.
- [13] B. Hille 3rd (Eds.), *Ion Channels of Excitable Membranes*, Sinauer Associates Inc., 2001, pp. 1–814.
- [14] J.L. Hindmarsh, R.M. Rose, A model of neuronal bursting using three coupled first order differential equations, *Proc. R. Soc. London B* 221 (1984) 87–102.
- [15] A.L. Hodgkin, The local changes associated with repetitive action in a non-modulated axon, *J. Physiol. (London)* 107 (1948) 165–181.
- [16] A.L. Hodgkin, A.F. Huxley, A qualitative description of membrane current and its application to conduction and excitation in nerve, *J. Physiol. (London)* 117 (1952) 500–544.
- [17] E.M. Izhikevich, Neural excitability, spiking and bursting, *Int. J. Bifurcation Chaos* 10 (6) (2000) 1171–1266.
- [18] H. Kawakami, Bifurcation of periodic responses in forced dynamic nonlinear circuits: computation of bifurcation values of the system parameters, *IEEE Trans. Circuits Systems CAS-31* (3) (1984) 248–260.
- [19] H. Kawakami, Y. Ozaki, Analysis of a separatrix loop in n -dimensional autonomous system, *IEICE Trans. J67-A* (11) (1984) 1098–1099 (in Japanese).
- [20] S. Kim, H. Kook, S.G. Lee, M.H. Park, Synchronization and clustering in a network of three globally coupled neural oscillators, *Int. J. Bifurcation Chaos* 8 (4) (1998) 731–739.
- [21] S. Kim, S.G. Lee, H. Kook, J.H. Shin, Phase dynamics of two and three coupled Hodgkin–Huxley neurons under DC currents, in: J.H. Oh, C. Kwon, S. Cho (Eds.), *Neural Networks: The Statistical Mechanics Perspective*, World Scientific, Singapore, 1995, pp. 141–155.
- [22] C. Koch, Phase space analysis of neuronal excitability, in: C. Koch (Ed.), *Biophysics of Computation: Information Processing in Single Neurons*, Oxford University press, New York, 1999, pp. 172–192.

- [23] Y.A. Kuznetsov, Two-parameter bifurcations of equilibria in continuous-time dynamical system, in: Y.A. Kuznetsov 2nd (Eds.), *Elements of Applied Bifurcation Theory: Applied Mathematical Science*, vol. 112, Springer, New York, 1998, pp. 293–392.
- [24] S.G. Lee, S. Kim, H. Kook, Synchrony and clustering in two and three synaptically coupled Hodgkin–Huxley neurons with a time delay, *Int. J. Bifurcation Chaos* 7 (4) (1997) 889–895.
- [25] C.M. Macica, L.K. Kaczmarek, Casein kinase 2 determines the voltage dependence of the Kv3.1 channel in auditory neurons and transfected cells, *J. Neurosci.* 21 (4) (2001) 1160–1168.
- [26] C. Morris, H. Lecar, Voltage oscillations in the barnacle giant muscle fiber, *Biophys. J.* 35 (1981) 193–213.
- [27] J. Nagumo, S. Arimoto, S. Yoshizawa, An active pulse transmission line simulating nerve axon, *Proc. IRE* 50 (1962) 2061–2070.
- [28] D. Noble, The development of mathematical models of the heart, *Chaos Solitons Fractals* 5 (1995) 321–333.
- [29] M. Nomura, T. Fukai, T. Aoyagi, Synchrony of fast-spiking interneurons interconnected by GABAergic and electrical synapses, *Neural Comput.* 15 (2003) 2179–2198.
- [30] L.S. Pontryagin (Ed.), *Ordinary Differential Equations*, Addison-Wesley, Reading, MA, 1962.
- [31] J. Rinzel, in: W.E. Fitzgibbon III, H.R. Walker (Eds.), *Research Notes in Mathematics, Nonlinear Diffusion*, Pitman, London, 1977.
- [32] J. Rinzel, G.B. Ermentrout, Analysis of neuronal excitability and oscillations, in: C. Koch, I. Segev 2nd (Eds.), *Methods in Neuronal Modeling: From Ions to Networks*, MIT Press, London, 1999, pp. 251–292.
- [33] M.E. Rush, J. Rinzel, Analysis of bursting in a thalamic neuron model, *Biol. Cybernet.* 71 (1994) 281–291.
- [34] M.E. Rush, J. Rinzel, The potassium A-current, low firing rates and rebound excitation in Hodgkin–Huxley models, *Bull. Math. Biol.* 57 (1995) 899–929.
- [35] P.N. Steinmetz, A. Roy, P.J. Fitzgerald, S.S. Hsiao, K.O. Johnson, E. Niebur, Attention modulates synchronized neuronal firing in primate somatosensory cortex, *Nature* 404 (2000) 187–190.
- [36] K.J. Swartz, Towards a structural view of gating in potassium channels, *Nat. Rev. Neurosci.* 5 (2004) 905–916.
- [37] F. Takens, Singularities of vector fields, *Publ. Math. IHES* 43 (1974) 47–100.
- [38] Z. Tiran, A. Peretz, B. Attali, A. Elson, Phosphorylation-dependent regulation of Kv2.1 Channel activity at tyrosine 124 by Src and by protein-tyrosine phosphatase epsilon, *J. Biol. Chem.* 278 (19) (2003) 17509–17514.
- [39] K. Tsumoto, T. Yoshinaga, K. Aihara, H. Kawakami, Bifurcations in synaptically coupled Hodgkin–Huxley neurons with a periodic α -function train, *Int. J. Bifurcation Chaos* 11 (4) (2001) 1053–1064.
- [40] E. Vaddla, I. Haalman, M. Abeles, H. Bergman, Y. Prut, H. Slovlin, A. Aertsen, Dynamics of neuronal interactions in monkey cortex in relation to behavioral events, *Nature* 373 (9) (1995) 515–518.
- [41] W.M. Yamada, C. Koch, P.R. Adams, Multiple channels and calcium dynamics, in: C. Koch, I. Segev 2nd (Eds.), *Methods in Neuronal Modeling: From Ions to Networks*, MIT Press, London, 1999, pp. 137–170.
- [42] T. Yoshinaga, H. Kawakami, Bifurcation and chaotic state in forced oscillatory circuits containing saturable inductors, in: L. Pecora, T. Carroll (Eds.), *Nonlinear Dynamics in Circuits*, World Scientific, Singapore, 1995, pp. 89–119.
- [43] T. Yoshinaga, Y. Sano, H. Kawakami, A method to calculate bifurcations in synaptically coupled Hodgkin–Huxley equations, *Int. J. Bifurcation Chaos* 9 (7) (1999) 1451–1458.